

AB-INITIO INVESTIGATION INTO THE PHYSICAL CHARACTERISTICS OF CuInSe₂ AND CuInTe₂ COMPOUNDS

Yousra Megdoud^{b,c}, Yamina Benkrima^{a*}, Redha Meneceur^f, Latifa Tairi^{c,d}, Abdelghani Lakel^e, Sebti Ghemid^e, Hocine Meradji^e

^a Ecole Normal Supérieur de Ouargla, 30000 Ouargla, Algeria

^b Institute of Sciences, University Center of Tipaza, Morsli Abdallah, Algeria

^c LPR Laboratory, Département of Physics, Faculty of Science, Badji Mokhtar –Annaba-Address, Algeria

^d Research Center in Industrial Technologies, CRTI, P.O. Box 64, Cheraga16014 Algiers Algeria

^e Laboratory of Metallic and Semiconducting, Materials, University of Biskra, BP 145 RP, 07000, Biskra, Algeria

^f Unit for the Development of Renewable Energies in Arid Zones (UDERZA), El Oued University, Algeria

*Corresponding Author e-mail: b-amina1@hotmail.fr

Received: September 3, 2023; revised November 05, 2023; accepted November 10, 2023

In this study, an analysis of chalcopyrite compounds CuInTe₂ and CuInSe₂ is presented, with a focus on their electronic, structural, optical, and thermal properties. The full-potential linearized augmented plane wave (FP-LAPW) method is employed for the investigation of these properties, based on a first-principles approach rooted in density functional theory (DFT). Two distinct approximations for the exchange and correlation potential, namely the WC-GGA and mBJ-GGA approximations, are considered in our calculations to ensure a robust and accurate examination of the materials under scrutiny. The findings obtained closely align with previously established theoretical and experimental data, thereby validating the reliability of our computational methodology. It is noteworthy that a novel dimension is introduced by this study, as the influence of both pressure and temperature on the thermal parameters of CuInTe₂ and CuInSe₂ compounds is explored. This facet of the research is distinguished by its innovative nature, as there is no prior record, to the best of our knowledge, of a similar analysis in the existing literature. The thermal properties are deemed of paramount significance, particularly in the context of crystal growth process optimization and the prediction of performance under extreme thermodynamic conditions.

Keywords: Photovoltaic; Chalcopyrite; FP-LAPW; Bandgap; Thermal properties

PACS: 73.20.At, 78.20.Ci

1. INTRODUCTION

In the domain of optoelectronics, two principal facets of material interest reside in the domains of light emission and the manifestation of the photovoltaic or photoelectric effect [1]. For applications encompassing luminous sources such as light-emitting diodes or laser diodes, an inherent prerequisite dictate that the material in question assume the role of a direct gap semiconductor. The wavelength of emitted light, and by extension, its color, intimately hinges upon the energy gap characterizing the constituents forming the p-n junction. Amidst the pantheon of energy sources, the sun emerges as the preeminent fount, characterized by its unparalleled abundance and unwavering reliability [2]. Consequently, the focal point has gravitated toward the development of solar energy converters through photovoltaic mechanisms. For materials earmarked for integration into solar cells, a pivotal criterion necessitates the possession of a high absorption coefficient, thereby favoring a substantial direct gap, ideally in proximity to 1.4 eV, to adeptly capture light across the visible spectrum [3]. Historically, the pervasive impediments of high costs and diminished efficiency have relegated solar cells to the fringes of ubiquitous everyday utility. Nevertheless, the evolving landscape has witnessed a proliferation of inquiry into novel materials primed for photovoltaic technology, coupled with advancements in solar cell fabrication techniques. Conventional stalwarts such as amorphous or crystalline silicon and cadmium telluride (CdTe) have shared the limelight alongside chalcogenides I-III-VI₂ in the realm of photovoltaic applications. Notably, a distinct focus has been channeled towards the intensive investigation of CuInSe₂ and CuInTe₂, endowed with high capacitance, and thus, proficient in light absorption [4]. Facilitated by electrochemical depositions, these compounds are predominantly harnessed in solid solution synergy with CuInSe₂ and CuInTe₂, fostering the creation of thin film solar cells with commendable efficiencies scaling up to 20% [5]. Engendering further intrigue is the quest for alternative materials that not only mirror these properties but concurrently feature an optimal energy gap to optimize device efficiency. One promising avenue lies in the realm of II-IV-V₂ compounds, which serve as ternary analogs to binary III-V configurations, wherein the group III element undergoes substitution with constituents from groups II and IV. In the majority of III-V semiconductors, such substitutions invariably impart distortions upon the 1×1×2 super cell of the sphalerite structure, concomitantly recognized as the chalcopyrite structure, akin to CuInSe₂. In such configurations, the lattice parameter ratio c/a typically deviates slightly from 2, and the distortion parameter u diverges from the idealized value of 1/4. These deviations bestow fresh fundamental attributes upon materials, encompassing but not confined to facets of electronics, transport, and optics [6].

Cite as: Y. Megdoud, Y. Benkrima, R. Meneceur, L. Tairi, A. Lakel, S. Ghemid, H. Meradji, East Eur. J. Phys. 4, 231 (2023), <https://doi.org/10.26565/2312-4334-2023-4-29>

© Y. Megdoud, Y. Benkrima, R. Meneceur, L. Tairi, A. Lakel, S. Ghemid, H. Meradji, 2023; CC BY 4.0 license

Within the expanse of II-IV-V2 semiconductors, a profusion of possibilities awaits exploration, predicated upon the judicious selection of elements from groups II, IV, and V. Regrettably, scant literature dedication is afforded to chalcopyrites encompassing copper, with CuInSe₂ and CuInTe₂ comprising the sole subjects of inquiry. Moreover, an observable lacuna exists, bereft of both experimental and theoretical insights pertaining to Cu-In-V2 compounds, notwithstanding the promise they hold for structural, electronic, or optical investigations [7-9].

From the array of materials under consideration, our focus has been directed toward the CuInX₂ compounds, where X represents selenium (Se) or tellurium (Te). Notably, these compounds manifest themselves in the crystalline chalcopyrite phase [10, 11]. It is imperative to underscore that the compounds under investigation in this study have commanded attention in prior research endeavors. R.C. Gupta et al. [12] delved into the mechanical stability parameters characterizing chalcopyrites and pnictides, with a particular emphasis on their relevance to optoelectronic materials. In a separate endeavor, Hao Yu et al. [13] embarked on an integrated exploration, combining experimental methodologies with first-principles investigations, thereby unraveling the intricacies of lattice dynamics within thermoelectric CuInTe₂. Further contributions from the scientific community include the work of Guanwei Jia et al. [14], who scrutinized the synthesis of CdS/CuInSe₂ and CuInTe₂/CuInSe₂ nanorod heterostructures through catalyst-assisted solution-liquid-solid techniques.

Temperature-dependent phonon anharmonicity and thermal transport properties in CuInTe₂ were scrutinized by Hao Yu, et al. [15], providing invaluable empirical insights. Notably, theoretical examinations conducted by E. Mazalan, et al. [16] enriched our understanding, focusing on the crystal structures and bulk modulus of CuInX₂ compounds, where X encompasses sulfur (S), selenium (Se), and their binary combination (S-Se), vital in the context of solar cell absorbers.

The structure of this paper is delineated as follows: "Section 2" expounds upon the CuInSe₂ and CuInTe₂ ternary compounds, elucidated via the utilization of the Wien2K code, rooted in the density functional theory (DFT). The ensuing "Section 3" derives implications for the utilization of these materials within the realm of photovoltaic applications, predicated upon the results gleaned. Finally, "Section 4" culminates in a comprehensive summary of the paper's conclusions, accompanied by the listing of the corresponding author.

2. DETAILS OF CALCULATIONS

In the scope of this investigation, we conducted initial-principle computations, employing the theoretical foundation of density functional theory (DFT) and adopting the Full-Potential Linearized Augmented Plane Wave (FP-LAPW) methodology. These calculations were executed utilizing the computational code WIEN2k. [17,20].

In order to determine the overall energy properties of the crystalline materials under investigation, a deliberate selection was made to evaluate the exchange-correlation energy [21] and potential functional elements using WC-GGA (Wu-Cohen Generalized Gradient Approximation) approach [21]. This method guarantees a thorough comprehension of the electronic attributes of the materials. Furthermore, in pursuit of greater precision regarding the structure of the electronic band and the values of band gap energy, an innovative strategy was adopted. Specifically, the TB-mBJ exchange potential was harnessed, in conjunction with GGA for the correlation contribution [22,23]. This amalgamation of methodologies is instrumental in elucidating the electronic behavior of the compounds under investigation with heightened accuracy. The computational methodology encompassed the partitioning of the crystal unit cell into distinct regions, namely the (IR) and the atomic spheres mimicking muffin-tin (MT) geometries, precisely centered around atomic positions. Within the interstitial region, the basis set was systematically expanded using plane waves to furnish an elaborate depiction of electronic characteristics in this domain. Conversely, within the MT spheres, the basis set was formulated as a linear amalgamation of atomic-like wave functions intricately associated with spherical harmonics. In addressing the issue of charge density and potential treatment within the unit cell's distinct regions, it is essential to highlight our methodology. A key aspect involves setting specific parameters for truncating spherical harmonics. In this regard, we opted for values of $R_{MT}K_{max} = 8$, with K_{max} representing the maximum value of the reciprocal lattice vector found within the first Brillouin zone of reciprocal space. Simultaneously, R_{MT} signifies the average radii encompassing the atomic-like spheres situated at atomic nuclei. The consideration of spherical harmonics expansion encompassed the maximum angular momentum value, signified as $l_{max} = 10$. It is pivotal to underscore that no shape approximations were invoked throughout this computational regimen. Consequently, a comprehensive consideration of all electrons, inclusive of core electrons, was accommodated, warranting the nomenclature "all electrons/full potential methods." In addition, the treatment of core electrons was administered in a fully relativistic manner. To capture the relativistic effects, the computational protocol entailed considering the spherically symmetric potential and numerically solving the radial Dirac equation. In stark contrast, valence and semi-core states were treated in a scalar relativistic fashion. To ensure not only reasonable convergence but also the prevention of charge leakage from the core, prudent choices were made regarding the muffin tin (MT) radii for distinct atomic species. Specifically, the selected values for Cu, In, Se, and Te atoms were set at 2.0 atomic units (u.a), exemplifying an approach to encompassing core electron interactions. Furthermore, within the framework of Brillouin zone integration for total energy calculations, a selection of 99-k-points within the irreducible part of the Brillouin zone was made to substantiate the integrity of the computations.

In pursuit of achieving convergence within the self-consistent iteration process, the maximum value of G_{max} was systematically set at $12 (Ry)^{1/2}$ for the Fourier expansion of the charge density. This parameterization collectively yielded total energy calculations with convergence levels comfortably below 10^{-4} Ry.

3. RESULTS AND DISCUSSION

3.1. Structural properties

This section directs its attention to investigating the structural properties of the compounds under study, specifically CuInSe_2 and CuInTe_2 . These compounds are categorized within the I-III-VI₂ family, representing a superlattice structure that originates from the ZnS phase. In this arrangement, the group II elements found in ZnS, such as Zn ions, are systematically and interchangeably substituted with group I transition metal ions like Cu, along with group III ions, which are common semiconductors. Consequently, each anion, whether Te or Se, is intricately coordinated by two Cu ions and two In cations, as illustrated in Figure 1.

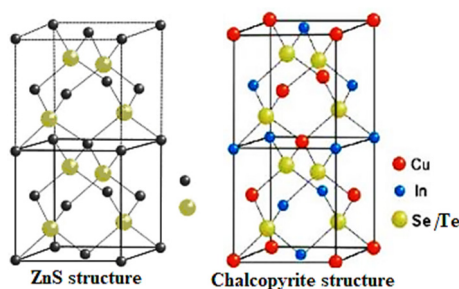


Figure 1. Crystalline structure of CuInSe_2 and CuInTe_2

Significantly, a four anions tetrahedral arrangement surrounds each Cu and In cation, mirroring the structural motif of ZnS. However, the systematic interchange of In and Cu cations within the square lattice introduces two notable structural deviations compared to the zinc-blende phase.

The first of these alterations manifests as a tetragonal distortion along the (001) direction, marked by a distortion parameter $\eta = c/2a$ [58], where η deviates from unity. This distortion arises due to dissimilar ionic radii between Cu and In cations.

The second structural modification arises from the presence of two distinct chemical bonds with unequal bond lengths within the tetrahedral framework, as depicted in Figure 1 (additional details provided in the supplementary materials). This complexity introduces a secondary form of distortion known as tetrahedral distortion.

In this distortion, Te and Se atoms are displaced from their idealized tetrahedral positions, defined as (1/4, 1/4, 1/4), thereby introducing an additional free parameter denoted as "u" within the chalcopyrite phase. It is noteworthy that in the zinc-blende phase, this parameter u remains fixed at 0.25. Here, u becomes intricately tied to the internal coordinates governing the positions of Te and Se anions.

These structural modifications result in a shift in the space group from $F4\bar{3}m$ (Space group of Zinc Blende structure) [58] to $I4\bar{2}d$ (Space group of Chalcopyrite structure) [58]. Within the chalcopyrite structure of these compounds, the Cu, In, Te, and Se atoms assume specific positions: (0, 0, 0), (0, 0, 0.5), and (u, 0.25, 0.125), respectively. To determine the equilibrium structural parameters of CuInSe_2 and CuInTe_2 using the WIEN2K package [17,20], our methodology encompassed several key steps. Initially, we computed the energy as a function of volume while maintaining the c/a ratio constant to ascertain the equilibrium volume. Subsequently, the c/a ratio was optimized by assessing its relationship with energy while maintaining the equilibrium volume established in the first phase. In the final phase, we minimized the parameter "u" using the Mini procedure, an integral component of WIEN2k [17,20]. Upon achieving minimized values for volume, c/a ratio, and "u," we obtained the optimal curve illustrating the total energy versus volume (See Fig 2).

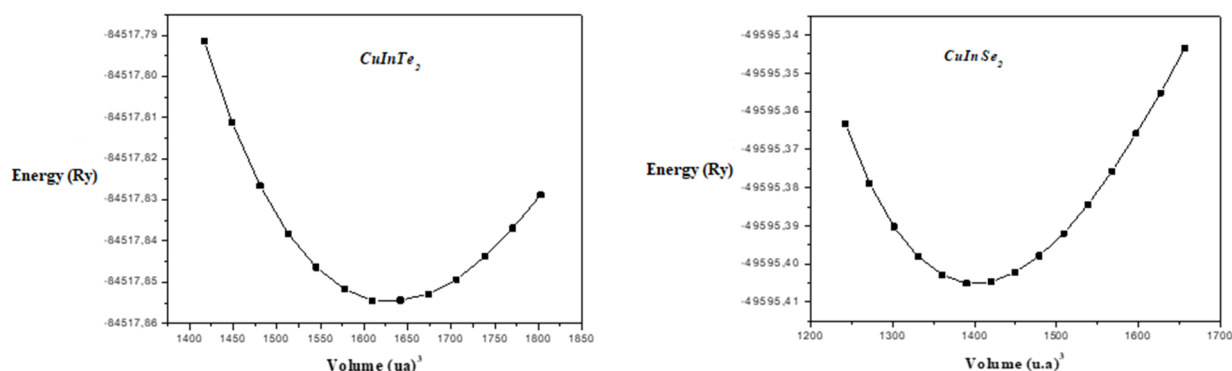


Figure 2. Total energy versus volume calculated for compounds CuInSe_2 and CuInTe_2

Using the Murnaghan equation of state (EOS) [24], we performed a curve fitting on this data. This allowed us to derive bulk modulus (B) and the equilibrium lattice constants (a and c). The calculated for the investigated compounds are presented in Table 1, alongside theoretical and other experimental results [12-16].

Table 1. Elastic Lattice parameters (a,c) (Å), compressibility modulus B (GPa), and its derivative B' of CuInSe₂ and CuInTe₂ compounds

Compounds		a (Å)	c (Å)	c/a	B(GPa)	B'
CuInSe ₂	Our calcs	5.84	11.671	1.99	53.8357	5.1027
	Exp	5.782 ^a	11.620 ^a	2.009	-	-
		5.78 ^b	11.62 ^b	2.010	-	-
		5.782 ^c	11.619 ^c	2.009	-	-
	Other calcul	5.836 ^d	11.657 ^d	1.997	54.236 ^d	5.364 ^d
		5.833 ^e	11.735 ^e	1.998	53.987 ^e	4.9875 ^e
CuInTe ₂	Our calcs	6.221	12.463	2.003	50.3970	4.8513
	Exp	6.197 ^f	12.453 ^f	2.009	-	-
		6.256 ^g	12.531 ^g	2.003	-	-
	Other calcul					

^aRef [8], ^bRef [9], ^cRef [10], ^dRef [11], ^eRef [12] ^fRef [13] ^gRef [14]

Notably, our findings obtained with the WC-GGA approximation closely align with experimental data and exhibit a higher degree of agreement compared to previous theoretical calculations. This concordance underscores the reliability of our theoretical results and instills confidence in the subsequent property calculations, given that these structural parameters serve as a foundational component of each subsequent computation. It is worth noting that the lattice parameters (a and c) exhibit a rise from CuInTe₂ to CuInSe₂. This increase in bond lengths corresponds to a weakening of bond forces, evident in the decreased bulk modulus ($B_{\text{CuInTe}_2} < B_{\text{CuInSe}_2}$). Importantly, the increase in lattice constants for these compounds from CuInTe₂ to CuInSe₂ is concomitant with a reduction in bulk modulus. The observed trend corresponds to the established relationship between bulk modulus (B) and lattice constant, as expressed by $B \propto V^{-1}$, with V representing the volume of the primitive cell [25].

3.2. Electronic properties

This section delves into an exploration of the electronic characteristics of CuInSe₂ and CuInTe₂, with a primary focus on the computation of energy band structures. Our calculations encompass the band structures of these compounds along high-symmetry lines within the first Brillouin zone, employing both the WC-GGA and mBJ approximations. As a representative illustration, Figure 3 showcases the computed band structures for CuInSe₂ and CuInTe₂.

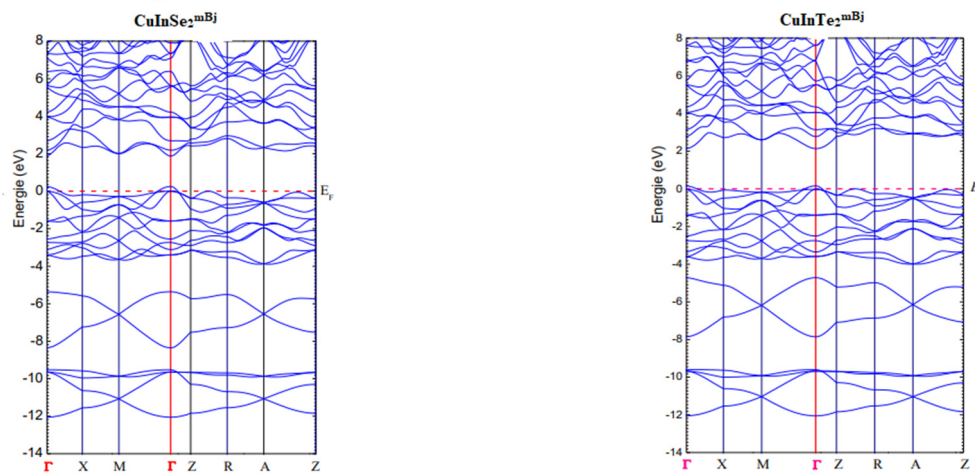


Figure 3. Calculated band structures of CuInSe₂ and CuInTe₂ compounds using the mBJ approximation

Across all compounds under investigation, a noteworthy consistency emerges: both the valence band maximum and the conduction band minimum are consistently situated at the Γ point. This arrangement engenders a direct energy gap for both CuInSe₂ and CuInTe₂. The specific values of the obtained band gaps are meticulously documented in Table 2, enabling a comprehensive comparison with preceding theoretical and experimental outcomes [12-16]. Crucially, the electronic band structures derived from the mBJ scheme bear qualitative resemblance to those obtained via the WC-GGA approximation. However, it is the quantitative aspect that truly sets them apart. The band gap values yielded by the mBJ approach significantly outperform those derived from the WC-GGA, drawing them closer to experimental data. It is widely recognized that mBJ represents a substantial enhancement over GGA concerning the accurate prediction of band gaps.

Table 2. Band gap value E_g for CuInSe₂ and CuInTe₂ with WC-GGA approximation and mBj

	E_g (eV) ($\Gamma - \Gamma$)			
	Our calculus		Experimental	Other calculus
	WC-GGA	mBj		
CuInSe ₂	0.75	1.03	1.01 ^a	0.99 ^a
CuInTe ₂	0.66	0.98	0.96 ^b	1.05 ^b

^aRef [15], ^bRef [16]

The mBJ approximation constitutes an enhancement in the treatment of potential exchange through the incorporation of a semi-local orbital [26]. Furthermore, hybrid functionals like B3PW91 [27] partially rectify the self-interaction error by introducing nonlocal Hartree-Fock (HF) exchange. It is worth noting that a consistent reduction in the bandgap is observed as the transition is made from CuInSe₂ to CuInTe₂, a trend that aligns with experimental observations [12-16]. This trend in bandgap reduction can be comprehended in light of our earlier analysis of structural characteristics. The expansion of lattice parameters (a, c) upon the substitution of Te for Se leads to a concomitant decrease in the bulk modulus (B) from CuInSe₂ to CuInTe₂, as visually depicted in Figure 3. These structural variations manifest as a reduction in the bandgap from CuInSe₂ to CuInTe₂. Additionally, the disparity in electronegativity between Te and Se further contributes to a subtle reduction in the bandgap.

3.3. Optical properties

The optical properties of solids provide valuable insights into the intricate interactions between electromagnetic waves and the electrons and ions within solid materials. At a microscopic level, these interactions can be precisely elucidated. However, to offer a macroscopic and quantitative description of these phenomena, the dielectric function $\epsilon(\omega)$ becomes indispensable. Mathematically, $\epsilon(\omega)$ is defined as $\epsilon(\omega) = \epsilon_1(\omega) + i\epsilon_2(\omega)$ [28-31]. Here, $\epsilon_2(\omega)$ is intricately linked to the electronic transitions responsible for absorption processes and can be meticulously computed by examining the momentum matrix elements that connect occupied and unoccupied electronic states [32]. On the other hand, $\epsilon_1(\omega)$ is intimately tied to polarization and can be derived from the imaginary part $\epsilon_2(\omega)$ through the well-established Kramers-Kronig relationships [33,34]. Using established mathematical relations, it's important to emphasize that one can directly derive all other optical constants, such as the absorption coefficient $\alpha(\omega)$ and the refractive index $n(\omega)$, from the components of the dielectric function.

Within the context of this research, the primary objective is to conduct an investigation into the optical properties of CuInSe₂ and CuInTe₂ utilizing the mBJ approach, with the aim of providing a comprehensive understanding of their significance in photovoltaic and other optoelectronic applications [21]. Notably, these materials exhibit anisotropy, originating from the electric field orientation perpendicular to the Oz axis (ϵ_{xy}), which signifies the average of spectra along the x and y directions, as well as the electric field aligned parallel to the Oz axis (ϵ_z). To characterize this anisotropy, the following relation is employed to determine the average value between the dielectric components ($\epsilon_{\perp c}$) and ($\epsilon_{\parallel c}$): $\epsilon = (2\epsilon_{\perp c} + \epsilon_{\parallel c})/3$. Importantly, it should be noted that this relation is equally applicable to other optical parameters.

3.3.1. The Dielectric Function's Real Part

Figure 4 showcases the real part of the dielectric function, $\epsilon_1(\omega)$, for CuInSe₂ and CuInTe₂ compounds, covering photon energies up to 40 eV.

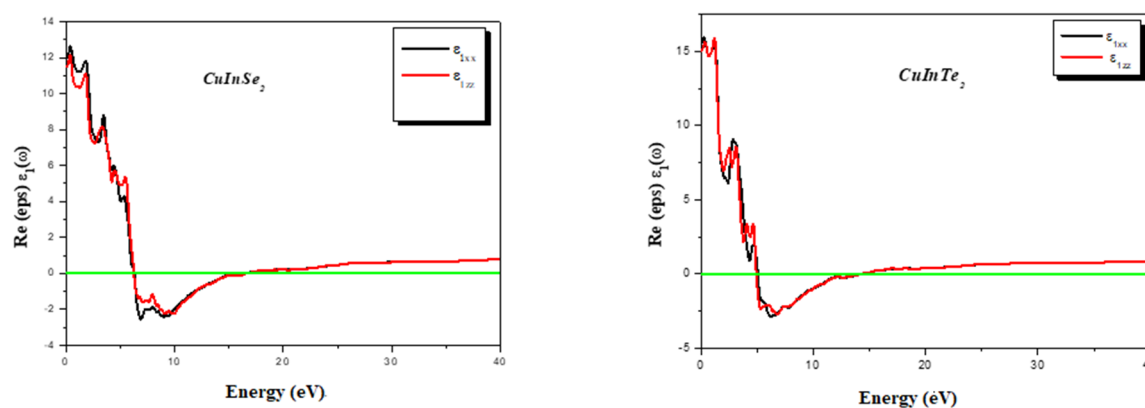


Figure 4. Calculated real parts of the complex dielectric constant for CuInSe₂ and CuInTe₂ compounds

These two compounds exhibit similar spectra, with an important observation that they both display isotropic behavior at lower energies. Notably, as depicted in Figure 4, the energy of the primary peak decreasing from 1.80 eV for CuInSe₂ to 1.55 eV for CuInTe₂. This shift in energy can be attributed to the electronic band structures of these compounds. Specifically, $\epsilon_1(\omega)$ reaches zero energy in the ultraviolet region, signifying the absence of dispersion [35]. Beyond this point, the spectrum progressively falls below unity in the ultraviolet (UV) range, ultimately surpassing unity at approximately 11.87 eV (CuInSe₂) and 15.08 eV (CuInTe₂). These frequencies correspond to the plasma frequency ω_p and are in alignment with the energy of the primary peak of energy loss [36]. Within the energy range where $\epsilon_1(\omega) < 0$, electromagnetic waves do not propagate, leading to a significant increase in the reflectivity of these compounds and inciting a metallic behavior [37]. This observation suggests that the investigated compounds (CuInSe₂ and CuInTe₂) could be employed for shielding against high-frequency electromagnetic waves [38]. In Table 3, we present a comprehensive summary of the static dielectric characteristics for the compounds under investigation, complemented by pertinent theoretical and experimental findings.

Table 3. Static Dielectric Function ($\epsilon_1(0)$) and Static Refractive Index ($n(0)$) Calculations for CuInSe₂ and CuInTe₂ Compounds

	n (0)		$\epsilon_1(0)$	
	Nos calcul WC-GGA	Autre calculs	Nos calcul WC-GGA	Autre calculs
CuInSe ₂	3.43	3.65	11.38	11.23
CuInTe ₂	3.87	3.95	15.01	15.23

^aRef [21]

It's important to highlight that $\epsilon_1(0)$ serves as an insightful metric, representing the electronic contribution to the static dielectric constant. This metric sheds light on the strength of interactions among electronic states within the valence and conduction bands when subjected to an external electric field. As a result, $\epsilon_1(0)$ is intricately linked to the energy gap value inherent to these compounds. Examining Table 3, it becomes evident that $\epsilon_1(0)$ increases from CuInSe₂ to CuInTe₂, a trend arising from the decreasing energy gap as one progresses from Se to Te. This relationship between the energy gap and $\epsilon_1(0)$ is governed by Penn's relation, which states that $\epsilon_1(0) \approx 1 + (\hbar\omega_p / E_g)$ [39], with $\hbar\omega_p$ representing the valence electron plasmon frequency. It's worth highlighting that the obtained values for $\epsilon_1(0)$ are consistent with prior theoretical findings. Although there is limited experimental data available for comparison, except for CuInTe₂ [40-41], our results closely align with the experimental work conducted by Wassim et al. [42] and Riede et al. [43].

3.3.2. The Dielectric Function's Imaginary Part

The dielectric function encompassing absorption phenomena, is displayed up to 40 eV in Figure 5. Importantly, it should be noted that consideration of indirect band transitions was intentionally omitted in our optical calculations. This exclusion is rooted in the fact that the influence of phonon scattering on dielectric screening, associated with indirect band transitions, is not significantly affected [44]. The critical energy point in $\epsilon_2(\omega)$, denoting the fundamental absorption edge, is observed at approximately 0.202 for CuInSe₂ and 0.485 for CuInTe₂. Within the context of this investigation, a noteworthy correlation emerges between the determined mBJ bandgap values for the compounds under scrutiny and the absorption edge. This absorption edge, in perfect accordance with the band structure, serves as the starting point for direct interband transitions at the Γ point. These transitions involve the highest occupied states of the valence band (BV) transitioning to the lowest unoccupied states of the conduction band (BC). Beyond the edge of absorption, as depicted in Figure 5, $\epsilon_2(\omega)$ undergoes a rapid increase. This increase is a consequence of the multitude of interband transitions that are present in the system. The principal peaks originate from direct interband transitions occurring between distinct levels within the conduction and valence bands. Notably, the energies associated with the maxima of these peaks are displaced towards lower values, specifically 5.89 eV for CuInSe₂ and 1.423 eV for CuInTe₂. This shift can be attributed to the differences in the underlying band structures of these two compounds.

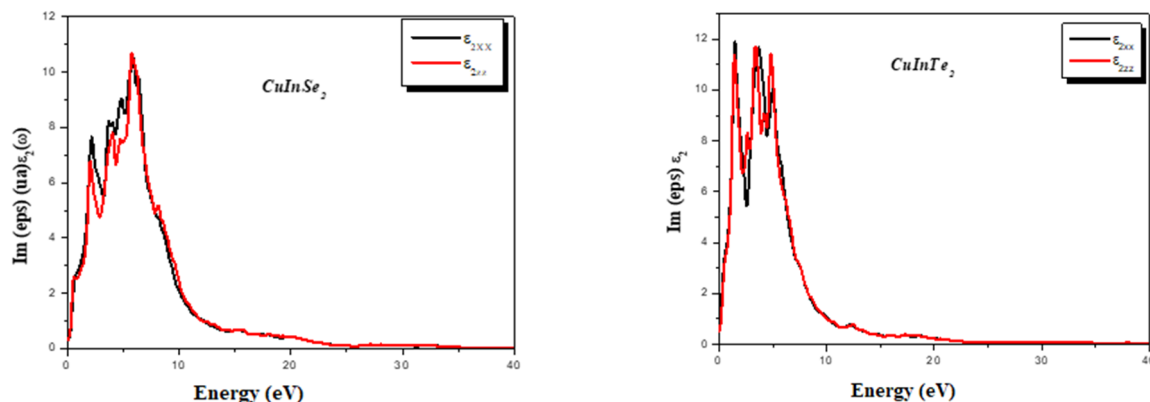


Figure 5. Computed Imaginary Parts of the Complex Dielectric Constant for CuInSe₂ and CuInTe₂ Compounds

3.3.3. The Refractive index

The refractive index [45], denoted as $n(\omega)$, represents a dimensionless number that provides a macroscopic depiction of the material's polarization response to incident electromagnetic waves, despite its microscopic origins. This refractive index is derived from the values of $\epsilon_1(\omega)$ and $\epsilon_2(\omega)$ [45]. Figure 6 illustrates the refractive indices for the compounds under investigation. It is noteworthy that $n(\omega)$ exhibits the same isotropic behavior as $\epsilon_1(\omega)$. The static refractive index values [46], determined using the equation $n(0) = \sqrt{\epsilon_1(0)}$ [46], closely align with those directly obtained from the refractive index plots for the compounds. Specifically, the values are 3.51 for CuInSe₂ and 4.03 for CuInTe₂, as detailed in Table 3. Furthermore, Table 3 highlights that the static values of $n(0)$ increase as we transition from CuInSe₂ to CuInTe₂. This behavior mirrors the increase observed in $\epsilon_1(0)$, attributable to the diminishing band-gap (E_g). According to Penn's relation, the band-gap (E_g) and, subsequently, $n(0)$ are inversely proportional [47-49].

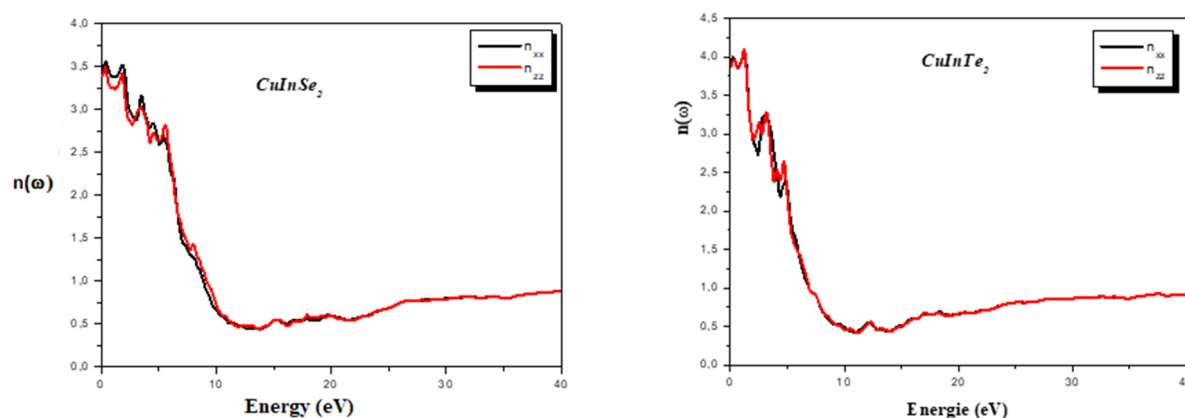


Figure 6. Variation of Refractive Index $n(\omega)$ for CuInTe₂ and CuInSe₂ Compounds

Our determined refractive indices closely align with prior theoretical investigations, underlining the consistency of our findings. An intriguing characteristic of chalcopyrite compounds is their inherent anisotropy, which results in birefringence. This birefringence imparts exceptional nonlinear optical properties to our studied compounds, enabling phase matching through a simple adjustment of the crystal's orientation concerning the incident beam [49]. This unique attribute positions our compounds ideally for applications in second harmonic generation (SHG) and optical parametric oscillation (OPO) [48, 49]. These favorable attributes lay a strong foundation for the potential development of high-performance laser systems utilizing our researched compounds.

3.3.4. Absorption coefficient

In the realm of photovoltaic conversion, photoconductivity, which involves the generation of charge resulting from incident radiation absorption, plays a pivotal role. The material's ability to allow light of a specific wavelength to penetrate before absorption hinges on the absorption coefficient—a crucial parameter for evaluating the potential of our compounds in visible spectrum photovoltaic conversion [58].

To investigate the suitability of our compounds for photovoltaic applications in the visible spectrum, the absorption coefficient $\alpha(\omega)$ up to 40 eV have been depicted in Figure 7. These optical features can be deduced from the real and imaginary components of the dielectric function [49].

In Figure 7, the absorption $\alpha(\omega)$ threshold, indicating the direct band gap (E_g), is found to be approximately 0.30 eV for CuInSe₂ and 0.09 eV for CuInTe₂. Based on these findings, it can be inferred that CuInTe₂ and CuInSe₂ compounds are better suited for harnessing the visible spectrum for photovoltaic conversion. Our compounds exhibit transparency and low reflectivity below the absorption threshold.

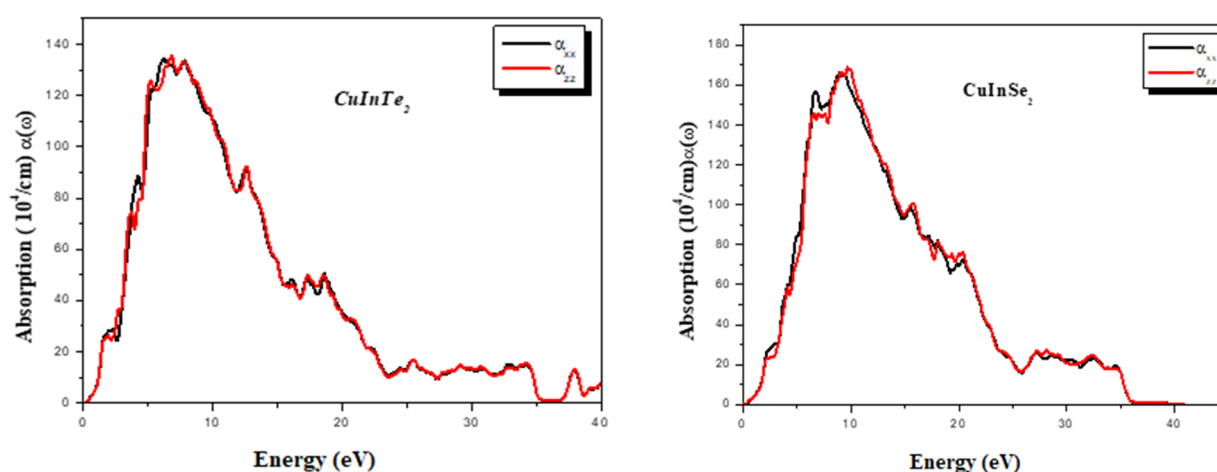


Figure 7. Calculated absorption coefficient $\alpha(\omega)$ versus energy (eV) for CuInSe₂ and CuInTe₂ compounds.

3.3.5. The Reflectivity spectrum

Figure 8 portrays the reflectivity behavior of our investigated compounds across an energy spectrum spanning 0-40 eV. Notably, the curves exhibit prominent peaks at 48% around 9.84 eV for CuInSe₂ and 49% at 8.02 eV for CuInTe₂. These findings strongly indicate the potential suitability of our ternary compounds for applications in the visible light range.

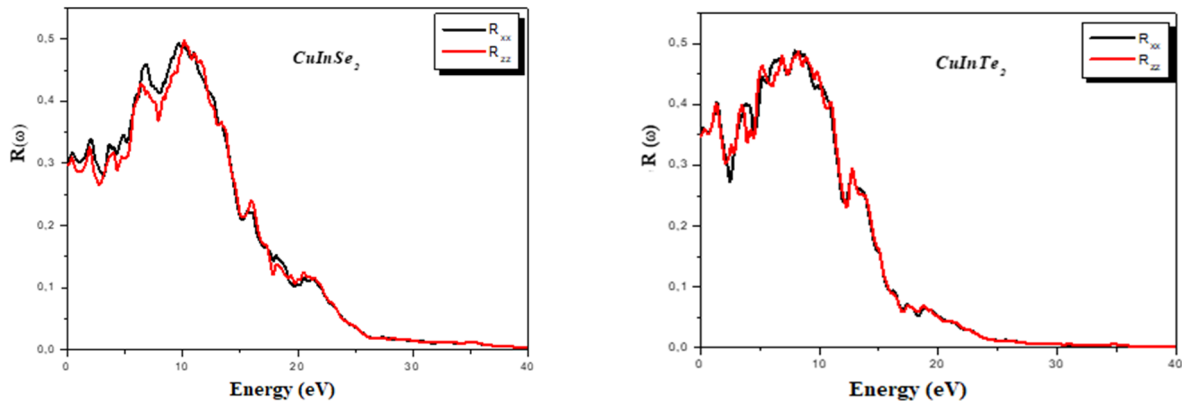


Figure 8. Reflectivity $R(\omega)$ Variation for CuInSe_2 and CuInTe_2 Compounds

3.4. Thermal properties

The investigation of thermal properties is fundamental in the realm of solid-state physics and various technological applications. Investigating how materials respond to high-pressure or high-temperature conditions allows us to gain insights into their unique behavior. In our research, we delve into the impact of temperature on the thermal properties of semiconductor materials, specifically CuInSe_2 and CuInTe_2 . In pursuit of this objective, we utilize a Gibbs program [50] built upon the quasi-harmonic Debye model. This approach empowers us to delve into the thermal characteristics of these compounds. The non-equilibrium Gibbs function, denoted as $G^*(V, P, T)$, is formulated as the sum of various components. These components encompass the total energy $E(V)$, the imposition of hydrostatic pressure PV , and the vibrational Helmholtz free energy A_{vib} .

$$G^*(V, P, T) = E(V) + PV + A_{\text{vib}}(T, \theta(V)) \quad (1)$$

Utilizing Debye's model for the phonon density of states, we can represent the vibrational term (A_{vib}) as follows: [51, 52]:

$$A_{\text{vib}}(\theta, T) = nk_B \left[\frac{9\theta}{8T} \right] + 3 \ln(1 - e^{-\theta/T}) D(\theta/T) \quad (2)$$

Here, $D(\theta/T)$ and n denote the Debye integral and the number of atoms per formula unit, respectively. In the case of an isotropic solid, the expression for θ_D is given as follows [53]:

$$\theta_D = \frac{h}{k_B} [6\pi^2 V^{1/3} n]^{1/3} f(\sigma) \sqrt{\frac{B_S}{M}} \quad (3)$$

Here, M represents the molecular mass per unit cell, while B_S stands for the adiabatic compressibility modulus. We can estimate B_S by approximating it as the static compressibility [50]:

$$B_S \cong B_T V \left(\frac{d^2 E}{dV^2} \right) \quad (4)$$

The Poisson's ratio, denoted as $f(\sigma)$, is assigned a value of 0.25 [54, 55]. Consequently, we can proceed to minimize the unbalanced Gibbs function $G^*(V, P, T)$ with respect to the volume V in the following manner:

$$\left[\frac{\partial G^*(V, P, T)}{\partial V} \right] = 0. \quad (5)$$

The equilibrium curve $V(P, T)$ can be derived, allowing us to obtain the isothermal compressibility modulus (B_T), heat capacity (C_V), and thermal expansion (α) using the following method [50]:

$$C_V = 3nk \left[4D \left(\frac{\theta}{T} \right) - \frac{3\theta/T}{e^{\theta/T} - 1} \right], \quad (6)$$

$$S = nk \left[4D \left(\frac{\theta}{T} \right) - 3 \ln(1 - e^{-\theta/T}) \right], \quad (7)$$

$$\alpha = \gamma C_V / V B_T \quad (8)$$

By employing Debye's quasi-harmonic model, we conducted comprehensive calculations of the thermal properties across various pressure conditions for our materials. These calculations were based on the equilibrium data for the E-V

relationship, which we initially derived at $T = 0$ and $P = 0$ as part of the WC approximation - GGA. Our exploration of thermal properties encompassed a temperature range spanning from 0 to 1000 K, while we also examined the impact of pressure across a range of 0 to 6 GPa.

3.4.1. Heat capacity et constant volume C_V

The investigation of crystal heat capacity is a well-established domain within condensed matter physics [50-51]. Understanding the heat capacity of a substance not only furnishes crucial insights into its vibrational characteristics but also holds significance in various practical applications.

Figure 9 illustrates the change in heat capacity at constant volume, (C_V) as a function of temperature (T) under different applied pressures for CuInSe₂ and CuInTe₂ compounds. The C_V of the studied systems exhibits distinct behaviors contingent upon the temperature range considered. At elevated temperatures, it tends to approach the Dulong-Petit limit [56] ($C_V \approx 3R$ for monatomic solids). This behavior is a common trait shared by all solids at high temperatures. Conversely, at sufficiently low temperatures, it follows a proportionality to T^3 [57].

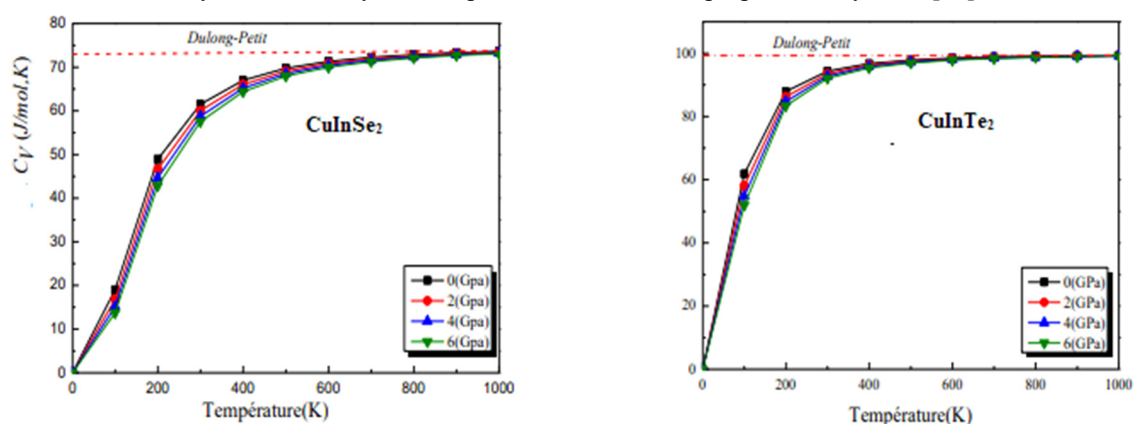


Figure 9. Variation of Specific Heat Capacity (C_V) with Temperature at Different Pressures for CuInSe₂ and CuInTe₂ Compounds

As shown in Figure 9, the heat capacity C_V significantly increases at low temperatures with rising temperature, after which the rate of increase becomes gradual at higher temperatures, eventually reaching the Dulong-Petit limit in accordance with theoretical expectations. The C_V values determined at $T=300$ K and $P=0$ GPa for CuInSe₂ and CuInTe₂ are 61.49 and 94.38 J/mol·K, respectively.

3.4.2. Thermal expansion α

The phenomenon of thermal expansion in solids is a ubiquitous yet often inconspicuous effect, concealing significant consequences. In a solid, atoms possess thermal energy and undergo vibrations around their equilibrium positions. These vibrations are temperature-dependent and are also influenced by the neighboring atoms, specifically, the interatomic potential generated by the surrounding atoms. At lower temperatures, these interatomic potentials can be approximated as harmonic, signifying that at temperatures close to $T = 0$ K, atoms remain centered around their mean position r_0 . However, as temperatures rise, the anharmonicity of interatomic potentials introduces a temperature-dependent shift in the average position of atoms, giving rise to the phenomenon of thermal expansion.

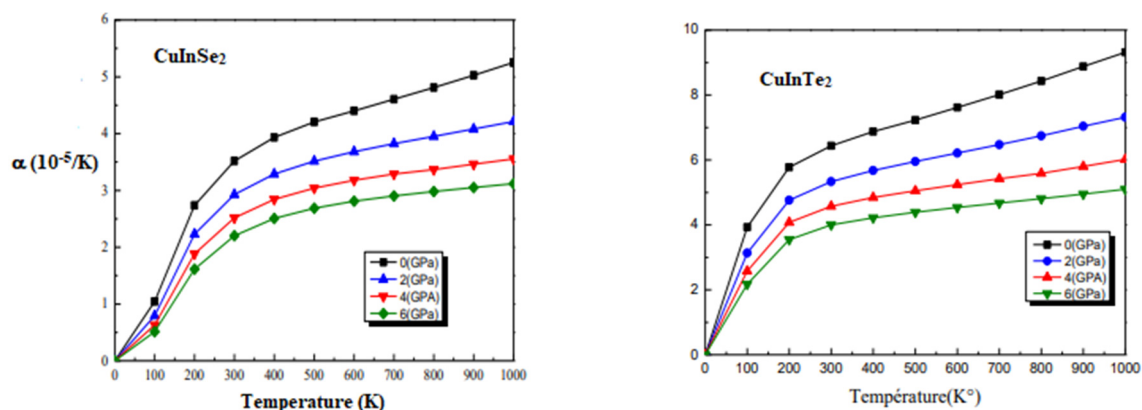


Figure 10. Variation of Thermal Expansion Coefficient (α) with Temperature at Different Pressures for CuInSe₂ and CuInTe₂ Compounds

The coefficient of thermal expansion characterizes the relationship between temperature and volume. As depicted in Figure 10, the variation in the coefficient of thermal expansion with temperature is illustrated at different pressures for the two ternary compounds, CuInSe₂ and CuInTe₂.

In the figure, it is observed that, at a given pressure, thermal expansion experiences a significant increase as temperature rises, up to approximately 200 K. Beyond $T > 200$ K, the thermal expansion rate gradually becomes more linear, suggesting that at high temperatures, thermal expansion is less influenced. Additionally, it's notable that thermal expansion is notably sensitive to temperature changes. At a given temperature, thermal expansion diminishes with increasing pressure. The calculated values of the coefficient of thermal expansion for CuInSe_2 and CuInTe_2 are $3.519 \times 10^{-5} \text{ K}^{-1}$ and $6.436 \times 10^{-5} \text{ K}^{-1}$ respectively.

3.4.3. The Debye temperature θ_D

The Debye temperature, a vital parameter tightly interconnected with a range of solid-state properties like specific heat and melting temperature, holds a key role in comprehending the behavior of solids. In Figure 11, we present the Debye temperature (θ_D) variation in response to temperature at different pressures for the two ternary compounds, CuInSe_2 and CuInTe_2 .

Upon closer examination of the figure, it becomes apparent that, while pressure remains constant, the Debye temperature gradually decreases in a nearly linear fashion as the temperature rises. Conversely, at a fixed temperature, the Debye temperature (θ_D) rises with applied pressure. This pattern aligns with the behavior observed in the evolution of the compressibility modulus concerning temperature and pressure. Significantly, it underscores the principle that harder materials typically exhibit higher Debye temperatures. Furthermore, under substantial applied pressure, the Debye temperature displays reduced sensitivity to changes in temperature.

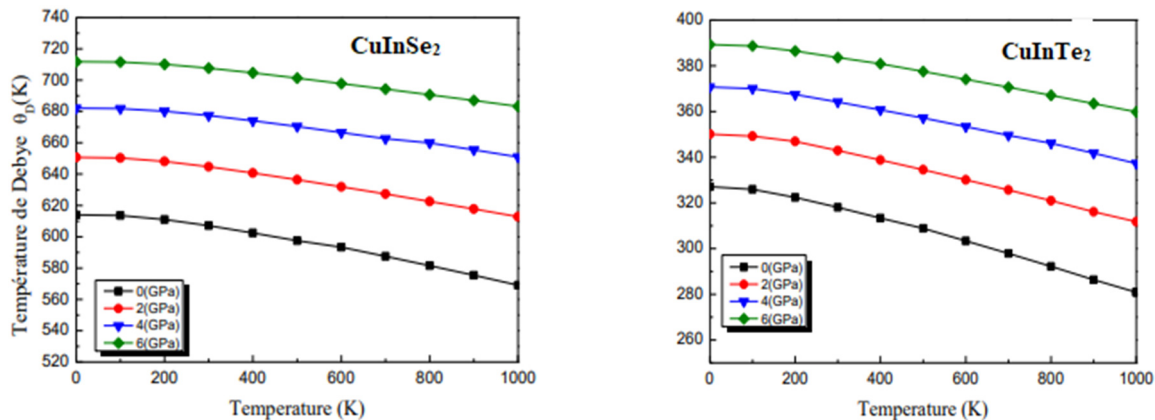


Figure 11. Variation of Debye Temperature (θ_D) with Pressure at Different Temperatures for CuInSe_2 and CuInTe_2 Compounds

3.4.4. The entropy of the system S

Entropy (denoted by the symbol S) is highly significant in describing the dispersion of energy and matter in systems. At the microscopic level, entropy functions as an indicator of the level of disorder within a system. Figure 12 illustrates the relationship between entropy (S), temperature, and pressure.

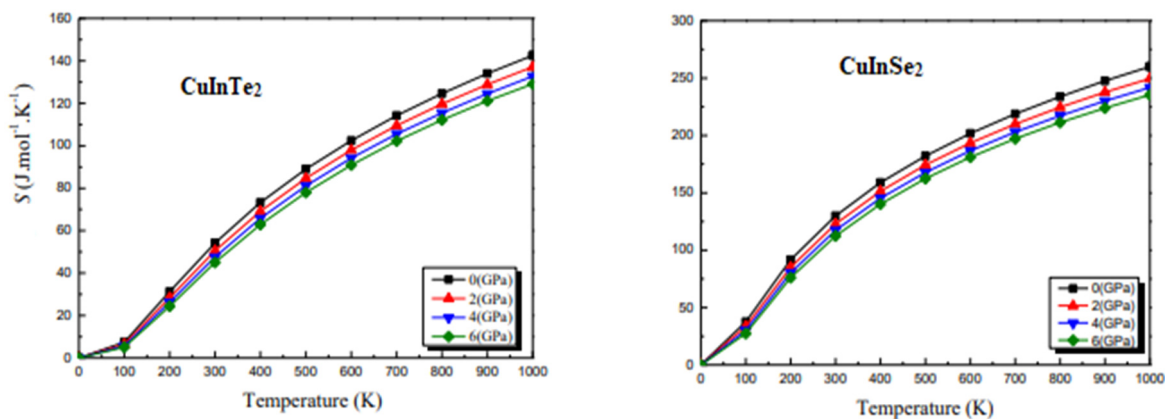







Figure 12. Entropy S versus pressure at various temperatures for CuInSe_2 and CuInTe_2 compounds

From the figure, it is evident that entropy exhibits a significant increase with rising temperature at a constant pressure, illustrating the system's tendency towards greater disorder as temperature climbs. Conversely, at a fixed temperature, entropy diminishes with increasing pressure, indicating a reduction in disorder under elevated pressure conditions. Notably, the calculated entropy values for CuInSe_2 and CuInTe_2 are 54.17 and 129.95 $\text{J/mol}\cdot\text{K}$, respectively.

4. CONCLUSION

In conclusion, our investigation employed the FP-LAPW approach within the WIEN2K code [17,20] to comprehensively explore the structural, optoelectronic, and thermal properties of CuInSe₂ and CuInTe₂ compounds. Our findings exhibited notable agreements with experimental data, surpassing previous theoretical research, particularly in terms of bandgaps, lattice parameters (a and c) and static optical parameters. Notably, we introduced a novel application potential for our compounds by analyzing their birefringence, showcasing their suitability for high-performance laser applications, a first within the domain of DFT-based research. Furthermore, our analysis of the absorption spectrum underscored the exceptional promise of CuInSe₂ and CuInTe₂ compounds for photovoltaic conversion within the visible range. Remarkably, we ventured into uncharted territory by investigating the thermal properties of these compounds using the Gibbs code, unveiling their suitability for extreme thermodynamic conditions, marking a significant contribution to the understanding of these materials.

ORCID

-  Hocine Meradji, <https://orcid.org/0000-0002-3359-3725>;
  Yamina Benkrima, <https://orcid.org/0000-0001-8005-4065>
 Abdelghani Lakel, <https://orcid.org/0000-0001-5098-849X>;
  Redha Meneceur, <https://orcid.org/0000-0002-1801-0835>
 Yousra Megdoud, <https://orcid.org/0000-0001-8999-8134>

REFERENCES

- [1] E. Rosencher, and B. Vinter, Structural Study, *Vibrational, Optical, Thermal Properties and Hirshfeld Surface Analysis of a New Iron (III) Complex Optoelectronics*, (Cambridge University Press, Cambridge, UK, (2002). <https://doi.org/10.1017/CBO9780511754647>
- [2] A. Luque, Will we exceed 50% efficiency in photovoltaics, *J. Appl. Phys.* **110**, 031301 (2011). <https://doi.org/10.1063/1.3600702>
- [3] R.H. Bube, *Photovoltaic Materials*, (Imperial College Press, London, 1998). [https://doi.org/10.1016/S1369-7021\(07\)70275-4](https://doi.org/10.1016/S1369-7021(07)70275-4)
- [4] W.N. Shafarman, and L. Stolt, in: *Handbook of Photovoltaic Science and Engineering*, edited by A. Luque, and S. Hegedus (Wiley, Chichester, UK, 2003) pp. 567–616. <http://dx.doi.org/10.1002/9780470974704.ch1>
- [5] M.A. Green, K. Emery, Y. Hishikawa, and W. Warta, “Solar cell efficiency tables,” *Prog. Photovolt: Res. Appl.* **18**, 346-352 (2010). <https://doi.org/10.1002/pip.1021>
- [6] S. Siebentritt, and U. Rau, editors, *Wide-Gap Chalcopyrites*, (Springer, Berlin, Heidelberg, Germany, 2006). https://link.springer.com/chapter/10.1007/3-540-31293-5_9
- [7] F. Chiker, B. Abbar, A. Tadjer, S. Bresson, B. Khelifa, and C. Mathieu, “Electronic structure and optical properties of ternary CdXP₂ semiconductors (X = Si, Ge and Sn) under pressure,” *Physica B*, **349**, 181-191 (2004). <https://doi.org/10.1016/j.physb.2004.03.087>
- [8] F. Chiker, B. Abbar, A. Tadjer, S. Bresson, B. Khelifa, and C. Mathieu, “The reflectivity spectra of ZnXP₂ (X=Si, Ge, and Sn) compounds,” *J. Solid State. Chem.* **177**(11), 3859-3867 (2004). <http://dx.doi.org/10.1016/j.jssc.2004.07.020>
- [9] B. Kocak and Y.O. Ciftci, “Ab-initio calculations of semiconductor,” *Mater. Res. Bull.* **77**, 300-306 (2016). <https://doi.org/10.1016/j.materresbull.2016.02.008>
- [10] Y. Marfaing, “Énergie photovoltaïque,” *J. Phys. IV France*, **12**, Pr 2 – 145 (2002). <https://doi.org/10.1051/jp420020021>
- [11] J. Müller, J. Nowoczin, and H. Schmitt, “Composition, structure and optical properties of sputtered thin films of CuInSe₂,” *Thin Solid Films*, **496**, 364-370 (2006). <https://doi.org/10.1016/j.tsf.2005.09.077>
- [12] R.C. Gupta, P. Varshney, Pravesh, M. Lal, D. Kumar, K. Singh, and A.S. Verma, “Mechanical stability parameters of chalcogenides and pnictides based optoelectronic materials,” *Chalcogenide Letters*, **20**(2), 101–112 (2023). <https://doi.org/10.15251/CL.2023.202.101>
- [13] H. Yu, G. Huang, Q. Peng, L.-C. Chen, H.-J. Pang, X.-Y. Qin, P.-F. Qiu, et al., “A combined experiment and first-principles study on lattice dynamics of thermoelectric CuInTe₂,” *Journal of Alloys and Compounds*, **822**, 153610 (2020). <https://doi.org/10.1016/j.jallcom.2019.153610>
- [14] G. Jia, and J. Du, “Catalyst-Assisted Solution–Liquid–Solid Synthesis of CdS/CuInSe₂ and CuInTe₂/CuInSe₂ Nanorod Heterostructures,” *Inorg. Chem.* **58**(1), 695-702 (2018). <https://doi.org/10.1021/acs.inorgchem.8b02870>
- [15] H. Yu, L.-C. Chen, H.-J. Pang, P.-F. Qiu, Q. Peng, and X.-J. Chen, “Temperature-dependent phonon anharmonicity and thermal transport in CuInTe₂,” *Physical Review B*, **105**, 245204 (2022). <https://doi.org/10.1103/PhysRevB.105.245204>
- [16] E. Mazalan, M.S.A. Aziz, N.A.S. Amin, F.D. Ismail, M.S. Roslan, and K. Chaudhary, “First-principles study on crystal structures and bulk modulus of CuInX₂ (X = S, Se, S-Se) solar cell absorber,” *Journal of Physics: Conference Series*, **2432**, 012009 (2023). <http://dx.doi.org/10.1088/1742-6596/2432/1/012009>
- [17] O.K. Anderson, “Linear methods in band theory,” *Phys. Rev. B*, **42**, 3060 (1975). <https://doi.org/10.1103/PhysRevB.12.3060>
- [18] P. Hohenberg, and W. Kohn, “Inhomogeneous Electron Gas,” *Phys. Rev. B*, **136**, 864 (1964). <https://doi.org/10.1103/PhysRev.136.B864>
- [19] W. Kohn, and L.S. Sham, “Self-Consistent Equations Including Exchange and Correlation Effects,” *Phys. Rev. A*, **140**, 1133 (1965). <https://doi.org/10.1103/PhysRev.140.A1133>
- [20] P. Blaha, K. Schwarz, G.K.H. Madsen, D. Kvasnicka, J. Luitz, *Wien2k. An Augmented Plane Wave Local Orbitals Program for Calculating Crystal Properties*, (Vienna University of Technology, Vienna, 2001).
- [21] Z. Wu, and R.E. Cohen, “More accurate generalized gradient approximation for solids,” *Phys. Rev. B*, **73**, 235116 (2006). <https://doi.org/10.1103/PhysRevB.73.235116>
- [22] F. Tran, and P. Blaha, “Accurate Band Gaps of Semiconductors and Insulators with a Semilocal Exchange-Correlation Potential,” *Phys. Rev. Lett.* **102**, 226401 (2009). <https://doi.org/10.1103/PhysRevLett.102.226401>
- [23] A.D. Becke, and E.R. Johnson, “A simple effective potential for exchange,” *J. Chem. Phys.* **124**, 221101 (2006). <https://doi.org/10.1063/1.2213970>
- [24] F.D. Murnaghan, “The Compressibility of Media under Extreme Pressures,” *P. Natl. Acad. Sci. USA*, **30**, 244-247 (1944). <https://doi.org/10.1073/pnas.30.9.244>

- [25] M.L. Cohen, "Calculation of bulk moduli of diamond and zinc-blende solids," *Phys. Rev. B*, **32**, 7988 (1985). <https://doi.org/10.1103/PhysRevB.32.7988>
- [26] S.N. Rashkeev, and W.R.L. Lambrecht, "Second-harmonic generation of I-III-VI₂ chalcopyrite semiconductors: Effects of chemical substitutions," *Phys. Rev. B*, **63**, 165212 (2001). <https://doi.org/10.1103/PhysRevB.63.165212>
- [27] A.D. Becke, "Density-functional thermochemistry. III. The role of exact exchange," *J. Chem. Phys.* **98**, 5648-5652 (1993). <https://doi.org/10.1063/1.464913>
- [28] J.S. Toll, "Causality and the Dispersion Relation: Logical Foundations," *Phys. Rev.* **104**, 1760 (1956). <https://doi.org/10.1103/PhysRev.104.1760>
- [29] L.D. Landau, and E.M. Lifshitz, *Electrodynamics of Continuous Media*, (Pergamon Press, Oxford, 1960). <https://doi.org/10.4236/ib.2011.33034>
- [30] H. A. Kramers, *Collected Science Papers* (North-Holland Publishing Co, Amsterdam, 1956). <https://doi.org/10.1088/0953-4075/38/13/016>
- [31] R. de L. Kronig, "Mean-Field Formulation of Maxwell Equations to Model Electrically Inhomogeneous and Isotropic Media," *J. Opt. Soc. Am.* **12**, 547 (1926). <https://doi.org/10.4236/ajcm.2018.84023>
- [32] C.M.I. Okoye, "Theoretical study of the electronic structure, chemical bonding and optical properties of in the paraelectric cubic phase," *J. Phys.* **15**, 5945 (2003). <https://doi.org/10.1103/PhysRevB.62.8828>
- [33] P.Y. Yu, and M. Cardona, *Fundamentals of Semiconductors*, (Springer, Berlin, 1996). http://dx.doi.org/10.1007/3-540-26475-2_1
- [34] A.H. Reshak, et al., "First Principle Study of Electronic Structure, Chemical Bonding and Optical Properties of 5-azido-1H-tetrazole," *J. Alloys Compd.* **509**, 6737 (2011). [http://dx.doi.org/10.1016/S1452-3981\(23\)12986-5](http://dx.doi.org/10.1016/S1452-3981(23)12986-5)
- [35] C.S. Schnorr, "Compound semiconductor alloys: From atomic-scale structure to bandgap bowing," *Appl. Phys. Rev.* **2**, 031304 (2015). <https://doi.org/10.1063/1.4930002>
- [36] Z. Lv, C. Cheng, Y. Cheng, X. Chen, G. Ji, "Elastic, thermodynamic and electronic properties of LaF₃ under pressure from first principles," *Computational Materials Science*, **89**(15), 57-64 (2014). <https://doi.org/10.1016/j.commatsci.2014.03.011>
- [37] R. de L. Kronig, "On the theory of dispersion of x-rays," *J. Opt. Soc. Am.* **12**, 547-557 (1926). <http://dx.doi.org/10.1364/JOSA.12.000547>
- [38] A. Shankar, R.K. Thapa, and P.K. Mandal, "Electronic and optical properties of CuInTe₂," *J. Phys. Conf. Ser.* **765**, 012008 (2016). <http://dx.doi.org/10.1088/1742-6596/765/1/012008>
- [39] D.R. Penn, "Wave-number-dependent dielectric function of semiconductors," *Phys. Rev.* **128**, 2093 (1962). <https://doi.org/10.1103/PhysRev.128.2093>
- [40] S.M. Wasim, and J.G. Albornóz, "Electrical and optical properties of n- and p-type CuInTe₂," *Phys. Status Solidi A*, **110**, 575-583 (1988). <https://doi.org/10.1002/pssa.2211100231>
- [41] J.G. Davis, P.M. Bridenbaugh, and S. Wagner, "Electrical and optical properties of copper indium ditelluride crystals grown from near-stoichiometric compositions," *J. Electron. Mater.* **7**, 39-45 (1978). <https://doi.org/10.1007/BF02656019>
- [42] V. Riede, H. Neumann, H. Sobotta, R.D. Tomlinson, E. Elliott, and L. Howarth, "Infrared study of lattice and free carrier effects in p-type CuInTe₂ single crystals," *Solid State Commun.* **33**, 557 (1980). [https://doi.org/10.1016/0038-1098\(80\)90859-5](https://doi.org/10.1016/0038-1098(80)90859-5)
- [43] N. Vermeulen, et al., "Post-2000 nonlinear optical materials and measurements: data tables and best practices," *Journal of physics photonics*, **5**(3), 035001 (2023). <https://doi.org/10.1088/2515-7647/ac9e2f>
- [44] N.V. Smith, "Photoelectron energy spectra and the band structures of the noble metals," *Phys. Rev. B*, **3**, 1862 (1971). <https://doi.org/10.1103/PhysRevB.3.1862>
- [45] F. Wooten, *Optical Properties of Solids*, (Academic Press, New York and London, 1972). [https://doi.org/10.1016/0169-4332\(90\)90007-M](https://doi.org/10.1016/0169-4332(90)90007-M)
- [46] A. Ghosh, R. Thangavel, and M. Rajagopalan, "Electronic and optical modeling of solar cell compound CuXY₂ (X = In, Ga, Al; Y = S, Se, Te): first-principles study via Tran-Blaha-modified Becke-Johnson exchange," *J. Mater. Sci.* **50**, 1710-1717 (2015). <http://dx.doi.org/10.1007/s10853-014-8732-z>
- [47] J.T. Goldstein, D.E. Zelmon, A.W. Saxler, S.M. Hegde, J.D. Wolf, P.G. Schunemann, et al., "Infrared properties of a nonlinear optical chalcopyrite semiconductor," *J. Appl. Phys.* **86**, 94 (1999). <http://dx.doi.org/10.1063/1.370704>
- [48] P.A. Franken, A.E. Hill, C.W. Peters, and G. Weinreich, "Generation of optical harmonics," *Phys. Rev. Lett.* **7**, 118 (1961). <https://doi.org/10.1103/PhysRevLett.7.118>
- [49] H. Salehi, and E. Gordanian, "Ab initio study of structural, electronic and optical properties of ternary chalcopyrites emiconductors," *Mat. Sci. Semicon. Proc.* **47**, 51-56 (2016). <https://doi.org/10.1016/j.mssp.2016.02.015>
- [50] R.R. Reddy, Y.N. Ahammed, K.R. Gopal, and D.V. Raghuram, "Optical electronegativity and refractive index of materials," *Opt. Mater.* **10**(2), 95-100 (1998). [https://doi.org/10.1016/S0925-3467\(97\)00171-7](https://doi.org/10.1016/S0925-3467(97)00171-7)
- [51] S. Cui, W. Feng, H. Hu, Z. Feng, and Y. Wang, "First principles studies of phase stability, electronic and elastic properties, computational Materials Science," **47**(4), 968-972 (2010). <https://doi.org/10.1016/j.commatsci.2009.11.030>
- [52] K. Bouamama, P. Djemia, N. Lebga, and K. Kassali, "High Pressure Macromolecular Crystallography," *High Pressure Research*, **27**(2), 269-277 (2007). <https://doi.org/10.1080/08957950701265359>
- [53] M.A. Blanco, A.M. Pendas, E. Francisco, J.M. Recio, and R. Franco, "Thermodynamical properties of solids from microscopic theory: applications to MgF₂ and Al₂O₃," *J. Mol. Struct. Theochem.* **368**, 245-255 (1996). [https://doi.org/10.1016/S0166-1280\(96\)90571-0](https://doi.org/10.1016/S0166-1280(96)90571-0)
- [54] E. Francisco, J.M. Recio, M.A. Blanco, A.M. Pendas, and A. Costales, "Quantum-Mechanical Study of Thermodynamic and Bonding," *J. Phys. Chem.* **102**, 1595-1601 (1998). <https://doi.org/10.1021/jp972516j>
- [55] E. Francisco, M.A. Blanco, and G. Sanjurjo, "Nontrivial effect of spin-orbit coupling on the intrinsic resistivity of ferromagnetic gadolinium," *Phys. Rev. B*, **107**, 115101 (2023). <https://doi.org/10.1103/PhysRevB.107.115101>
- [56] V.Kh. Kozlovskiy, "To the Question of Validity Grüneisen Solid State Equation," *World Journal of Condensed Matter Physics*, **2**(4), (2012). <http://dx.doi.org/10.4236/wjcmp.2012.24038>
- [57] A. T. Petit, and P. L. Dulong, "Recherches sur Quelques Points Importants de la Théorie de la Chaleur," *Annales de Chimie et de Physique*, **10**, 395-413 (1819). http://www.ffn.ub.es/luisnavarro/nuevo_maletin/Petit--Dulong_1819.pdf

- [58] R. Mahdjoubi, Y. Megdoud, L. Tairi, H. Meradji, Z. Chouahda, S. Ghemid, and F. El Haj Hassan, "Structural, electronic, optical and thermal properties of CuXTe (X=Al, Ga, In) compounds: an study," International Journal of Modern Physics B, 33(07), 1950045 (2019). <http://dx.doi.org/10.1142/S0217979219500450>

AB-INITIO ДОСЛІДЖЕННЯ ФІЗИЧНИХ ХАРАКТЕРИСТИК СПОЛУК CuInSe₂ І CuInTe₂

Юсра Мегдуд^{b,c}, Яміна Бенкріма^a, Редхе Менесер^f, Латіфа Таїрі^{c,d}, Абдельгані Лекле^e, Себті Гемід^c, Хосін Мераджі^c

^a Вища нормальна школа Уаргла, 30000 Уаргла, Алжир

^b Інститут наук Університетського центру Тіпаза, Морслі Абдаллах, Алжир

^c Лабораторія LPR, департамент фізики, факультет природничих наук, Баджі-Аннаба-Адрес, Алжир

^d Науково-дослідний центр промислових технологій ЦРТІ, П.О. Вох 64, Черага 16014, Алжир Алжир

^e Лабораторія металів та напівпровідників, матеріалів, Університет Біскри, ВР 145 РР, 07000, Біскра, Алжир

^f Відділ розвитку поновлюваних джерел енергії в посушливих зонах (UDERZA), Університет Ель-Уед, Алжир

У цій роботі представлений аналіз сполук халькопїриту CuInTe₂ та CuInSe₂ з акцентом на їх електронні, структурні, оптичні та термічні властивості. Для дослідження цих властивостей використовується повнопотенційний метод лінеаризованої приєднаної плоскої хвилі (FP-LAPW), заснований на підході перших принципів, що ґрунтується на теорії функціоналу щільності (DFT). У наших розрахунках враховуються два різні наближення для обмінного та кореляційного потенціалу, а саме наближення WC-GGA та mBJ-GGA, щоб забезпечити надійне та точне дослідження досліджуваних матеріалів. Отримані результати тісно узгоджуються із раніше встановленими теоретичними та експериментальними даними, тим самим підтверджуючи надійність нашої обчислювальної методології. Примітно, що це дослідження відкриває новий аспект, оскільки досліджується вплив тиску, так і температури на термічні параметри сполук CuInTe₂ і CuInSe₂. Цей аспект дослідження відрізняється своїм новаторським характером, оскільки, наскільки нам відомо, такого аналізу в існуючій літературі не було. Термічні властивості мають першорядне значення, особливо у контексті оптимізації процесу вирощування кристалів та прогнозування продуктивності в екстремальних термодинамічних умовах.

Ключові слова: фотоелектрика; халькопїрит; FP-LAPW; заборонена зона; теплові властивості